Journal of Materials Research and Technology 31 (2024) 1337–1354

Contents lists available at ScienceDirect

Journal of Materials Research and Technology

journal homepage: www.elsevier.com/locate/jmrt

Understanding the fatigue behaviour of Ti–6Al–4V manufactured via various additive processes

L. Ednie [a], A.A. Antonysamy [b], L. Parimi [b], M. Mani [b], M. Thomas [c], R.J. Lancaster [a,*]

[a] Institute of Structural Materials, Bay Campus, Swansea University, Swansea, SA1 8EN, UK
[b] GKN Global Technology Centre, Additive Manufacturing Group, Taurus Road – Patchway, Bristol, BS34 6FB, UK
[c] Interdisciplinary Programmes in Engineering, University of Sheffield, Mappin Street, Sheffield, S1 3JD, UK

ARTICLE INFO

Handling editor. P Rios

Keywords:
Ti-6Al–4V
Additive manufacture
Fatigue
Surface finish

ABSTRACT

Additive Manufacturing (AM) is receiving widespread attention from both industry and academia who are looking to benefit from the numerous advantageous possibilities that AM processes have to offer, such as the potential to design and produce highly complex bespoke geometries with minimal material wastage. Yet, despite this, AM also has some drawbacks. Some of the most significant include the presence of process-induced defects and the inherent surface roughness of an AM built component, both of which can have a considerable influence on the mechanical properties of the final product. This research will investigate the role of an as-built surface on the fatigue properties of AM Ti–6Al–4V manufactured by electron beam melting (EBM), laser powder bed fusion (L-PBF) and laser metal deposition with wire (LMD-w). Fatigue results have been generated alongside advanced surface profilometry, microstructural, defect and fractographic analyses that have revealed that whilst the surface roughness in the majority of instances is the primary factor impacting the fatigue performance on AM material, it cannot be considered alone. It was found that the inherent as-built (AB) surface finish was significantly different across the various AM processes, inducing a range of effective stress concentrations and thus, a contrasting impact on the resulting fatigue performance. Results from each variant have been compared against a machined and polished equivalent, to provide a further consideration as to whether the as-built surface would be suffice from a time and economical viewpoint. Statistical analysis of the generated results also allowed for an extrapolation of predicted fatigue lives in the very high cycle regime for the alternative AM Ti–6Al–4V variants.

1. Introduction

Additive manufacturing (AM) is an advanced manufacturing technique whose uptake within the aerospace industry is thought to be a key driver to reaching the UK imposed 2050 Net-Zero targets [1]. This is being driven by the advantages that the use of AM could unlock, including but not limited to, cost savings through reduced material usage, the ability to produce components with an increased geometrical complexity and the removal of bottlenecks within conventional manufacturing processes due to reduced manufacturing times. Whilst AM can unlock numerous benefits across multiple industries, its uptake is currently being limited due to several challenges and an uncertainty within the mechanical performance of AM components.

One of the main advantages AM could enable would be the ability to manufacture bespoke components ready made for direct placement within larger systems, but this is hindered by the high-surface roughness that is seen within as-built (AB) AM components. One of the main challenges is that there is currently a limited understanding of the role of the inherent surface roughness that is seen within AM built components and the effects of this on a component's mechanical performance, in particular, the cyclic fatigue properties [2]. It has also been found that there are limited standards available to help with the choice of appropriate post-processing methods to reduce the surface roughness of AM components [3]. It has been noted that less than 1 % of ISO/ASTM standards relate to surface finishing of AM parts [4].

The surface roughness of a sample or component can be defined as variations in height along the sample surface in relation to a reference plane [5]. It is known that the AB surface of an AM component is significantly rougher than that of a conventionally manufactured component. This is primarily due to a number of factors such as the staircase effect, incomplete melting of powder particles or the balling phenomenon [6], each of which vary from process to process and are

* Corresponding author.
E-mail address: r.j.lancaster@swansea.ac.uk (R.J. Lancaster).

https://doi.org/10.1016/j.jmrt.2024.06.168
Received 16 May 2024; Received in revised form 17 June 2024; Accepted 22 June 2024
Available online 24 June 2024

influenced by powder variables, process parameters and component geometries [7]. Incomplete melting of powder particles is seen when a lower energy input than is required is used. This results in there being insufficient energy to fully melt powder particles and results in solid powder particles being attached to the surface. Incomplete powder particle melting can cause an average surface roughness that is approximately the same as the diameter of the powder particles used to build the component. Likewise, it is also expected that metallic powders with a large diameter will be more difficult to melt completely than powders with a smaller diameter, therefore this will result in components produced using powder particles of large diameters having a greater surface roughness than when the same component is produced using powder particles of a smaller diameter [2].

The observable roughness conditions can subsequently impact the components' mechanical properties [8–10]. It has been noted in a number of studies that whilst the surface roughness of a component can have a significant impact on its mechanical properties, it cannot be considered alone, and that a number of other factors should be considered including the component orientation, microstructure and process-induced defects, such as porosity [11–13].

Ti–6Al–4V, otherwise recognised as Grade 5 titanium, is a popular material for AM, with many published sources documenting the alloys production using various AM processes, including Electron Beam Melting (EBM) [14], Laser Powder Bed Fusion (L-PBF) [15] and Directed Energy Deposition (DED) [16]. Each of these processes have subtle differences. For instance, both EBM and L-PBF utilise a heat source to sinter metallic powder on a heated base plate to construct a component layer-by-layer, but as given by the initial term of each process, the nature of the heat source is different. Whereas in DED, a focused energy source is used to melt and fuse material as it is deposited, and the process is commonly used for repair and cladding based applications. Therefore, the main difference between DED and the two powder bed processes is that L-PBF and EBM melt the material before it is being deposited, while the melting process in DED takes place during the deposition of powder. Such differences can have a subsequent impact on the surface roughness, and in turn, the fatigue properties of the material.

Being able to solve the challenge of surface roughness is of high importance as it one of the most important features when producing intricate components that are commonly seen within the aerospace industry. If components were to be produced using AM for a high-end application, they would typically require an average surface roughness that is less than 3.2 μm. Whilst the high-surface roughness of AM components cannot be completely removed through the optimisation of process parameters or powder variables, it can be reduced using methods of post-processing such as machining and polishing [6]. Therefore, there is a need to fully understand the effects of the as-built surface roughness on the fatigue properties of materials produced through different AM processes, without nullifying the benefits of each respective manufacturing method.

The aim of this study is to investigate the effects of the inherent AM surface roughness on the fatigue performance of the titanium alloy Ti–6Al–4V. Ti–6Al–4V samples will be manufactured using various AM methods including EBM, L-PBF and Laser Metal Deposition with Wire (LMD-w), with samples built in different orientations and assessed in both the AB and machined & polished (M&P) surface condition. Experimental results will be supported by advanced surface profilometry, microstructural, defect and fractographic analysis, with predictions of longer fatigue lives provided from statistical analysis methods.

2. Experimental methods

2.1. Material

In this research, Ti–6Al–4V fatigue specimens were manufactured through a series of additive processes, namely: EBM, L-PBF and LMD-w, with an additional batch of specimens extracted from the wrought Ti–6Al–4V baseplate used for the manufacture of L-PBF samples.

2.1.1. Electron beam melting (EBM)

Cylindrical EBM samples were built on a theme 5.0 ARCAM Q20+ machine using virgin Ti–6Al–4V powder, with the nominal composition given in Table 1. During manufacture, both the electron beam column and the vacuum chamber are initially pressurised to a base pressure of $5x10^{-5}$ mbar or lower which is maintained until an inert gas is introduced into the chamber at $4x10^{-3}$ mbar.

A series of vertically (90°) built specimens were manufactured with a volumetric energy density of 50 J/mm^3. The specimens were fabricated with a build layer thickness of 90 μm, a particle size distribution ranging between 42 and 102 μm and an apparent powder density of 2.54 g/cm^3, taken from three separate powder batch measurements. EBM parameters used to programme the ARCAM Q20+ such as the build chamber pre-heat temperature and electron beam spot size were inline with those suggested by ARCAM, and are given in Table 2.

The dimensions of the EBM Ti–6Al–4V specimens were manufactured in accordance with the measurements stated in BS EN6072:2010 [18]. Half of the samples were manufactured to remain with an AB surface condition, whereas the other half were built with a stock addition of 1.52 mm. This excess material allowed for these samples to be M&P to a mirror like finish while ensuring all samples had the same final dimensions prior to axial fatigue testing.

Post manufacture, all samples were subjected to a hot isostatic pressing (HIP) treatment (920 °C ± 10 °C, 102 MPa for 120 min) to reduce the presence of any internal features such as porosity which could have an adverse effect on the cyclic properties.

2.1.2. Laser powder bed fusion (L-PBF)

A series of vertically orientated (90°) four-point bend (4 PB) L-PBF specimens were manufactured and finished in one of two different surface conditions. This included AB and M&P. The specimens were produced using gas-atomised virgin Ti–6Al–4V powder with a powder particle size between 20 and 63 μm and an apparent density of 2.41 g/cm^3, taken from three separate powder batch measurements. This powder was melted together to produce the final components using an EOS M290 machine with a single 400 W laser. The process parameters used for this L-PBF build are detailed in Table 3.

Post manufacture, once the specimens were safely removed from the base plate, they were subjected to the appropriate post processing surface procedure. This included three of the four surfaces on each specimen being subjected to machine & polishing, whereas the fourth surface remained in the AB condition or subjected to M&P.

2.1.3. Laser metal deposition with wire (LMD-w)

The LMD-w process sees Ti–6Al–4V wire feedstock material being fed into the path of a laser which acts to melt the wire and results in the deposition of a bead of material onto a substrate or component for repair. At the beginning of this AM process, the power supplied by the laser to heat the wire feedstock also causes the substrate to melt, which produces a melt pool in the substrate which then mixes with the melted wire droplets, promoting the fusion of the substrate and wire material. The deposition of material droplets is continued until the desired geometry is achieved. The wire feedstock and high energy laser are held at suitable angles by a multiaxial robot, which is housed within an active vacuum cell.

In this research, LMD-w Ti–6Al–4V builds were manufactured with two separate sets of process parameters, one deemed to be 'parameter set 1', and the other 'parameter set 2'. The process parameters for the

Table 1
Nominal composition of Ti–6Al–4V alloy (wt.%).

Al	V	Fe	C	N	O	Ti
6.57	3.96	0.20	0.01	0.01	0.20	Bal

Table 2
ARCAM EBM process parameters [17].

Parameter	ARCAM Suggested Value
Environment	Vacuum, 10^{-4}-10^{-5} (mbar)
Pre-heating (°C)	700 (powder bed heating by unfocused electron beam)
Maximum beam power (W)	3500
Electron beam spot (μm)	200–1000
Average powder layer thickness (μm)	50–200
Beam scan speed (m/s)	>1000

Table 3
L-PBF process parameters.

Parameter	Value
Hall flow rate (s/50 g) for powder	22
Oxygen level of powder (%)	0.15
Nitrogen level in powder (%)	0.01
Build plate area (mm x mm)	250 x 250
Energy density (J/mm^3)	25
Layer thickness (μm)	80
Baseplate material	Ti–6Al–4V
Baseplate heating (°C)	200
Powder rake	Silicone

parameter set 1 build can be seen in Table 4. Due to the proprietary nature of the LMD-w process, the process parameters of the parameter set 2 build cannot be disclosed at this stage, but it can be inferred that the parameter set 1 LMD-w build was carried out under colder and slower conditions than the parameter set 2 LMD-w build.

LMD-w Ti–6Al–4V uniaxial cylindrical samples were manufactured in the vertical orientation whilst flat plate LMD-w Ti–6Al–4V samples were built in the horizontal orientation with parameter set 1 conditions. Both specimen batches were tested uniaxially and were finished with a M&P surface.

The LMD-w samples manufactured with parameter set 1 either consisted of a 4 PB test (with AB surface) or flat plate (M&P finish) geometry. The 4 PB samples remained with an AB surface with samples built in both the horizontal and vertical orientations, whilst horizontally orientated flat plate samples were also manufactured and finished with a M&P surface. Each of the respective specimen types complied with the dimensions described for the other AM Ti–6Al–4V variants.

2.1.4. Conventional Ti–6Al–4V

To allow a baseline comparison of the fatigue behaviour of additively manufactured material to a conventional counterpart, additional flat plate uniaxial specimens were extracted from the wrought Ti–6Al–4V base plate used for the manufacture of the L-PBF samples, and manufactured to the same dimensions to complement those produced through the various AM processes. The Ti–6Al–4V base plate was treated in accordance to specification AMS 4911.

2.2. Analytical methods

2.2.1. Surface roughness measurements

To characterise the surface roughness parameters of the specimens an Alicona Infinite Focus G5 was utilised. Post scan analysis was carried out using the Infinite Focus Measurement Suite by Alicona, which sees the use of a series of algorithms that analyse variations within the recorded optical images and results in 3D topographical data for the sample [19]. Four surface roughness measurements were taken at various positions around the circumference or face of the samples covering an area of approximately 13 x 2 mm. Various surface roughness parameters were recorded, and are listed in Table 5. Through the application of a plane and a l_c filter, the roughness parameter data gained is in line with ISO 21920–2:2021 [20], while the surface parameter data recorded is in accordance with, ISO 25178–2:2021 Areal Part 2 [21] and ISO 12781–1:2011 [22] standards. All measurements were carried out in compliance with ISO 21290 for roughness [20].

Table 4
Process parameters for parameter set 1 LMD-w Ti–6Al–4V build.

Parameter	Value
Laser Power (kW)	10
Wire Feed Speed (mm/s)	81.08
Robot Speed (mm/s)	11.04
Laser Spot Size (mm)	6.7

2.2.2. Microscopy

Optical microscopy for porosity imaging was carried out using a Zeiss Smartzoom 5 which allowed high magnification stitched images to be recorded. A Zeiss Evo LS25 scanning electron microscope (SEM) was also used for high magnification imagery of the fracture surfaces and the contrasting microstructures, from which microstructural measurements could be recorded including grain size and α lath width. All grain size measurements, for both α and β phases, were recorded manually using the mean linear intercept method, in line with ASTM E112-13 [23]. This was carried out using image analysis software (ImageJ), by drawing a line across an image of the sample microstructure, from which the line was then measured, and the number of grain boundary intersections were recorded. To increase the repeatability of this measurement, this measurement was carried out at multiple points across a micrograph to gain an average grain size value.

A Hitachi SU3500 SEM, with electron backscatter diffraction (EBSD) capability, was used to capture crystallographic texture maps. EBSD scans were acquired using a step size of 1.5 μm and 4 x 4 binning, with the band detection mode optimised for EBSD. EBSD data was acquired using the Tango plug-in included in the Channel 5 software.

2.3. Mechanical testing

2.3.1. Uniaxial fatigue testing

Uniaxial stress-controlled fatigue tests were performed on cylindrical EBM samples in the AB and M&P conditions, cylindrical LMD-w parameter set 1 vertical samples in the M&P condition, flat plate conventional samples with a M&P finish and both parameter sets 1 and 2 LMD-w horizontal flat plate samples with a M&P finish. The fatigue tests were carried out under load-controlled conditions using an Instron servo-hydraulic test machine with a load capacity of 100 kN. Cylindrical test pieces were subjected to a range of maximum applied stress values to generate a suitable maximum stress (σ_{MAX}) – number of fatigue cycles to failure (N_f) curve. Prior to testing, the diameter of each sample's gauge length was measured at multiple points using a shadow graph and the applied σ_{MAX} values were calculated in accordance with ISO Standard 1099:2017 for axial force-controlled fatigue testing of metallic materials [24].

The constant amplitude fatigue tests were carried out using a loading ratio of R = 0.1 and a frequency of 5 Hz under a sinusoidal load control waveform, at ambient room temperature. Run out was determined to be

Table 5
Definitions of surface roughness parameters generated from Alicona surface profiling.

Surface parameter	Surface parameter definition
R_a	Roughness of a profile (μm)
R_t	Maximum peak to valley height of roughness profile (μm)
R_p	Maximum peak height of roughness profile (μm)
MR^2	Fraction of a surface while will carry the load (%)
R_v	Maximum valley height of roughness profile (μm)
S_a	Average height of selected area (μm)

3,000,000 cycles, upon which the test was stopped. On the respective σ_{MAX} – N_f curve, a run out is indicated by an arrow.

2.3.2. Four-point bend fatigue testing

Four-point bend (4 PB) fatigue tests were carried out on AB LMD-w parameter set 2 vertical and horizontal samples, L-PBF vertical samples in both the AB and M&P conditions. The tests were performed under the same nominal conditions as the uniaxial fatigue tests, using an R-ratio of 0.1 and a frequency of 5 Hz under a sinusoidal load-controlled waveform, with all tests being performed at ambient room temperature. It should be noted that if the sample cracks or fails at one of the locations in contact with the supporting roller, then this results in the test being classed as void and discarded from any further analysis. Fig. 1 illustrates the configuration of the 4 PB fatigue tests. Additional 4 PB fatigue data on conventionally manufactured Ti–6Al–4V was also sourced from Ref. [25] to allow a baseline comparison to the AM materials.

3. Results

3.1. Material

3.1.1. Microstructure

Microstructural images of the different Ti–6Al–4V AM variants and the conventional equivalent are displayed in Fig. 2. The images show that the conventional material (Fig. 2m) has a microstructure consisting of primary α grains surrounded by β at the grain boundaries. It should be noted that this material was extracted from the build plate used for the manufacture of the L-PBF specimens and has subsequently been subjected to heat during the build process which could have possibly led to some coarsening of the grain structure. Despite this, the grain size of the AMS4911 Ti–6Al–4V material is relatively fine (13.85 μm) and is consistent with those documented in literature (5–20 μm) [26].

The various AM microstructures exhibit a relatively consistent grain morphology, typified by elongated columnar grains on the X-Z plane, parallel to the build direction. Such behaviour is attributed to the specific solidification and cooling processes that occur during the layer-by-layer additive process. More specifically, the material will undergo solidification as each layer is added, leading to a directional alignment of grains and subsequent anisotropy in the microstructure. As such, due to these complex thermal gradients, the resultant microstructure differs on the X–Y and X-Z planes, where the X–Y plane usually offers a more equiaxed morphology. This is indeed the case here in the various AM Ti–6Al–4V microstructures, where an ordered and equiaxed β microstructure can be seen, perpendicular to the build direction, while the X-Z plane shows evidence of a columnar β grain structure running parallel to the build direction. In the X–Y plane, a fine needle-shaped α lath morphology can be seen within the equiaxed β grain structure, which is then also seen within the columnar grain structure of the sample orientated within the X-Z plane. The α lath size in particular, is an important parameter to consider since it can influence the yield strength and fatigue life of Ti–6Al–4V. Lucas et al. previously found that as the α lath size decreases, the material yield strength increases which then gives rise to improved cyclic properties [27].

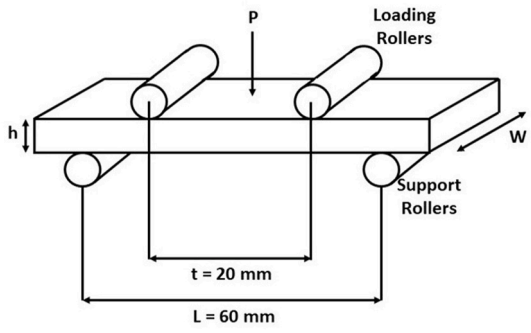

Fig. 1. Four-point bend fatigue test arrangement.

On either plane, the microstructures of each of the AM variants predominantly consist of an α lath structure, with a small amount of retained β phase at the α lath boundaries. The β phase can be seen retained within prior columnar β grains, which surround needle like α laths [28]. Due to the columnar nature of the prior β grains, random measurements were taken of the β grain widths across each of the respective planes. Likewise, for the α laths, width and length measurements were recorded. For each set of measurements, recordings were made from three images of each plane and averaged in line with ASTM E112-13 [23]. These measurements, alongside mean linear intercept measurements taken both horizontally and vertically across each image, have been included in Table 6 to allow a quantifiable comparison of the microstructures seen in Fig. 2.

As seen from the microstructural values, the L-PBF variant appears to have the largest α lath widths and lengths but the smallest prior β grain size of the AM materials, whilst the EBM material exhibits the largest α grain size. In contrast, the LMD-w materials, manufactured with either of the two parameter sets, have smaller microstructural features relating to the α phase, yet the largest prior β grain size. The difference in grain size between the L-PBF and EBM materials can be attributed to the distinct thermal characteristics and energy inputs associated with the respective additive process. The L-PBF build was manufactured on a pre-heated baseplate of approximately 200 °C. However, the base plate temperature of the EBM builds was significantly higher, at approximately 700 °C. This contrast in pre-heat temperature would induce a difference in the cooling characteristics of the two materials, where the EBM material would be expected to experience reduced temperature gradients during cooling and subsequently exhibit a coarser microstructure compared to L-PBF. On the contrary, due to the reduced base plate temperature during L-PBF manufacture, the material would experience more rapid heating and cooling rates thus promoting nucleation and reducing the level of grain growth. This is also the case for the LMD-w variants, which exhibit the smallest α phase measurements, since the single laser used during the process is highly localised and once the laser has passed, the recently melted material experiences limited convection from surrounding material due to the larger surface areas of the LMD-w flat plate specimens. Generally, there is little variation in the microstructures of the L-PBF and EBM materials, and a similar finding was reported by Nguyen et al. [6], who reviewed AM of Ti–6Al–4V as produced through EBM, L-PBF and DED.

Additional microscopy images were captured using EBSD. Fig. 3 presents inverse pole figure maps of the different AM microstructures on both the X–Y and X-Z planes. These maps allow for the determination of the crystallographic orientation of each sample, whilst the grain boundaries are more distinct. Looking at the various AM microstructures, there is minimal evidence of significant texture on either plane but a basketweave microstructure is more evident. The secondary α laths are also more apparent in the X-Z plane, which is typically a result of the high cooling rate experienced during the rapid solidification process of AM.

3.1.2. Surface profilometry

Surface roughness values were generated on each of the specimens tested. Previous studies have discussed the correlations that can be made between surface parameters and component fatigue life [29–31]. Qiu et al. [32] found that height-based roughness parameters produced the strongest correlation to fatigue life, and that surface data values such as R_a and R_t, were not sufficient metrics for quantifying fatigue performance in Inconel 718 [33]. In a more holistic and cross-cutting study, Sanaei et al. found that correlations between parameters such as R_p, MR^2, and R_v provided a stronger correlation to a materials' fatigue life than parameters such as R_a and R_t across an array of materials, including L-PBF Ti–6Al–4V [34]. Therefore, within this work, attention has been

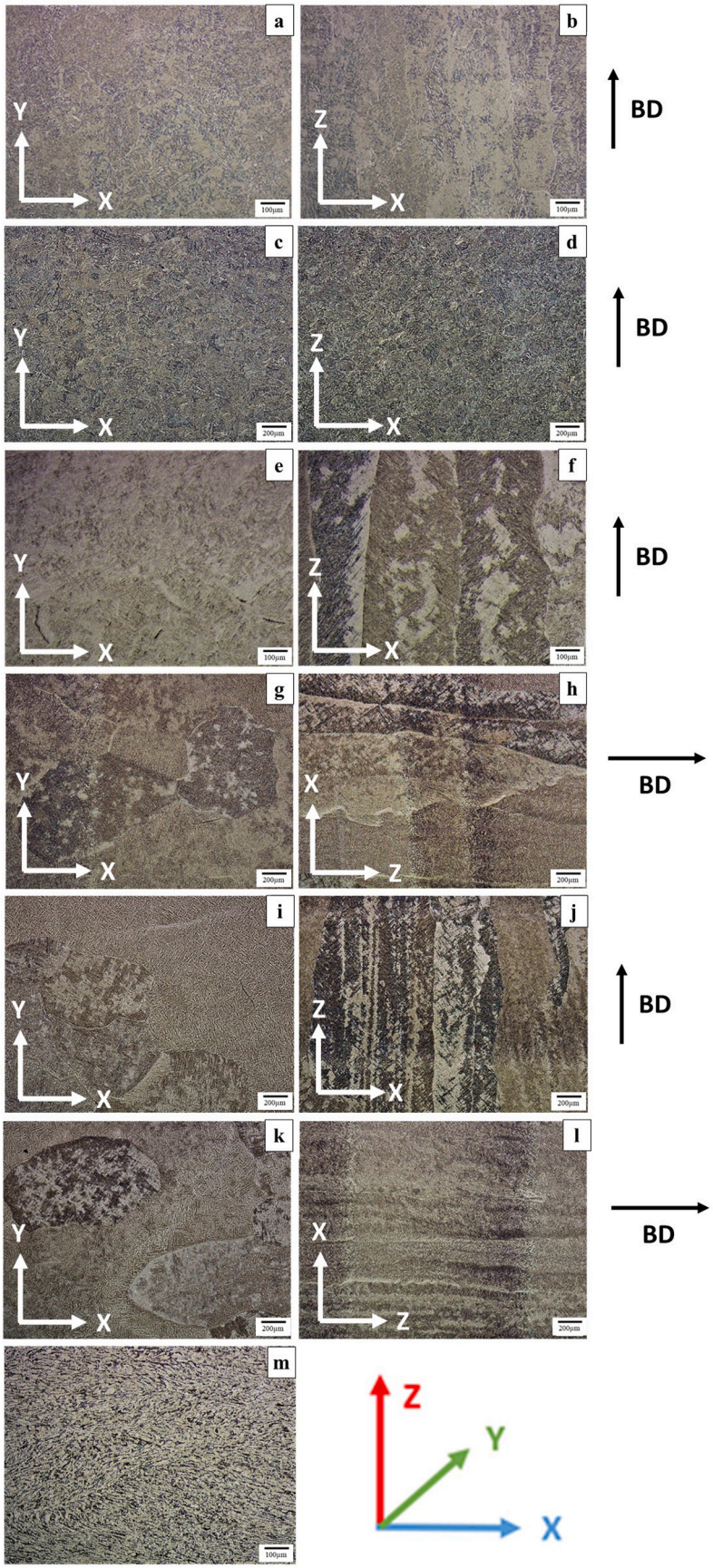

Fig. 2. Optical micrographs of Ti–6Al–4V material **a)** EBM vertical X–Y, **b)** EBM vertical X-Z, **c)** L-PBF vertical X–Y, **d)** L-PBF vertical X-Z, **e)** LMD-w parameter set 1 vertical X–Y, **f)** LMD-w parameter set 1 vertical X-Z, **g)** LMD-w parameter set 1 horizontal X–Y, **h)** LMD-w parameter set 1 horizontal X-Z, **i)** LMD-w parameter set 2 vertical X–Y, **j)** LMD-w parameter set 2 vertical X-Z, **k)** LMD-w parameter set 2 horizontal X–Y, **l)** LMD-w parameter set 2 horizontal X-Z, **m)** Conventional.

Table 6
Microstructural measurements of the different Ti–6Al–4V variants. PS1 refers to parameter set 1, PS2 refers to parameter set 2.

Material	Face	Average β Grain Size (μm)	Average α Grain Size (μm)	Average α Lath Width (μm)	Average α Lath Length (μm)	Aspect Ratio	Number of α laths measured	α lath area (μm^2)
EBM V	X–Y	188.46	4.00	2.09	12.23	0.885	3358	16.12
	X-Z	143.58	4.01	2.14	13.74	0.226	3118	16.87
L-PBF V	X–Y	153.33	1.91	2.74	31.45	0.849	2207	23.15
	X-Z	116.67	2.43	2.57	35.49	0.212	2114	24.72
LMD-w PS1	X–Y	115.57	0.84	1.02	14.46	0.708	10249	4.66
V	X-Z	294.12	1.23	1.40	18.52	0.258	3414	15.61
LMD-w PS1	X–Y	707.69	1.40	0.99	13.01	0.798	2647	24.82
H	X-Z	740.01	1.56	1.08	16.97	0.179	2005	27.25
LMD-w PS2	X–Y	884.62	0.88	1.33	21.75	0.725	3481	16.07
V	X-Z	415.38	0.68	1.24	19.41	0.156	6875	7.23
LMD-w PS2	X–Y	284.73	1.18	1.93	25.20	0.764	5590	8.73
H	X-Z	1292.31	0.92	2.04	18.51	0.120	6898	7.86
Conventional (Axial)		25.12	13.85	9.41	52.51	0.913		

paid to a selection of parameters that are most commonly renowned, and those that are understood to play the most critical role, including R_a, R_t, R_p, MR^2, R_v and S_a parameters. The definition for each of these parameters can be seen in Table 5. It should also be noted that other surface parameters were also considered within this study, but strong correlations were not noted.

A selection of the typical surface profiles recorded using the Alicona Infinite focus surface profilometer can be seen in Fig. 4, with the resulting average surface roughness parameters displayed in Table 7.

3.2. Fatigue results

The results from the fatigue tests on the different AM Ti–6Al–4V materials are presented in Fig. 5 in the form of stress v number of fatigue cycles to failure plots, or S–N curves, for the EBM, LMD-w parameter sets 1 and 2 and LPBF specimens, respectively. In each plot, the tests that surpassed 3,000,000 cycles and did not fail have been designated as run outs (as indicated by arrows) whilst some other tests were continued to failure. The trendlines in each plot have not included any tests that ran out, with the trendlines in each projected forward to 3,000,000 cycles to provide an indication of the approximate level of stress required to reach the fatigue limit.

As would be expected, the results indicate that generally the samples with a M&P surface finish outperform their AB equivalent due to the reduced number of stress concentration features at the surface. Of the samples with an AB surface finish, the process-induced surface roughness of the EBM Ti–6Al–4V material was found to have the most detrimental effect on the fatigue performance. This is clearly displayed in Table 8, which compares the fatigue lives of specimens tested under the same loading conditions (σ_{MAX} = 600 MPa). As shown, there is a considerable difference in fatigue life across the different AM Ti–6Al–4V variants, in the order of 1000x, and multiple factors need to be considered as potential reasons for such behaviours. These include the nature of the employed AM process, the build orientation, resulting microstructure, the fatigue test method used, surface finish and the resulting stress concentrations at the surface, and also the population and magnitude of any process-induced defects.

In each plot, fatigue results from conventional Ti–6Al–4V material have also been provided to allow a baseline comparison for each AM process. In each instance, the M&P AM variant has outperformed the fatigue performance of the conventional equivalent. However, caution should be taken when comparing the fatigue lives of the conventional material tested under axial conditions as opposed to those generated under 4 PB loading. The results from the 4 PB fatigue tests were gathered on a far more refined microstructure (2.2 μm) [25], leading to a far superior cyclic response compared to the material used for the axial tests. Given this, plus the differences in the loading behaviours (as will be discussed later), comparing the two S–N curves can not be considered a fair exercise.

When considering the effects of build orientation on the fatigue life of AM samples, this primarily relates to the microstructure that is formed during manufacture. For AM materials, due to the layer-by-layer manner of additive manufacture, an elongated, columnar grain structure is commonly observed in the epitaxial build direction. In contrast, in a horizontally orientated material, the columnar grains would be expected to travel across the cross-section of the material, perpendicular to the primary loading direction of an axial test-piece. Such a difference leads to anisotropic mechanical and cyclic properties, since fatigue crack growth in a vertically orientated sample would be expected to engage with a higher number of grain boundaries which subsequently hinder the rate of crack propagation, as opposed to the horizontal equivalent. Therefore, with the grain boundaries of these columnar grains slowing down the movement of the fatigue crack, it allows for the sample to withstand a greater number of cycles to failure, improving the fatigue life.

The effects of orientation can be seen in the fatigue life of samples tested at σ_{MAX} = 600 MPa. Direct comparisons between vertically and horizontally orientated samples can be seen with the LMD-w parameter set 1 M&P samples, with the vertically orientated sample achieving 630,147 cycles prior to failure, while the horizontally oriented equivalent only achieved 29,280 cycles. This difference in fatigue life between the two orientations sees the vertically orientated sample achieve a fatigue life ~21x that of the horizontally orientated equivalent. Whilst the M&P samples accurately reflect this difference in fatigue life due to differing orientations, the AB samples do not, implying that other factors such as surface roughness and internal defects also have a major influence on the fatigue behaviour. It is seen that with the AB LMD-w parameter set 2 samples, the horizontal sample has a fatigue life (41,032 cycles) greater than the vertically orientated sample (24,755 cycles). Therefore, this indicates that given the horizontally built samples are usually outperformed by the vertical equivalent for samples with a M&P surface, other influences should be considered.

One such factor is the contrasting test methodologies used, namely uniaxial fatigue, in the form of cylindrical and flat plate samples, and 4 PB fatigue tests. The biggest difference that is seen between the two test types is the distribution of stress within the samples. Within an axially loaded fatigue sample, the stress is distributed evenly throughout the gauge section of the sample whereas in a 4 PB fatigue sample, the stress is applied perpendicular to the test-piece, and this results in moments along the sample's length and gives a σ_{MAX} at the centre of the sample. It has been suggested in previous work by Shrestha et al. on LPBF stainless steel samples, that fatigue samples subjected to axial loading exhibited a lower fatigue resistance than samples that were subjected to cyclic bend testing [10]. This is to be expected, given that a uniaxial test-piece is more statistically envisaged to encounter a defect or irregularity than a bend test sample, considering the volume of material that is stressed in each test arrangement. Similar work was carried out by Imam et al. where a comparison of bending and axial loading fatigue tests was

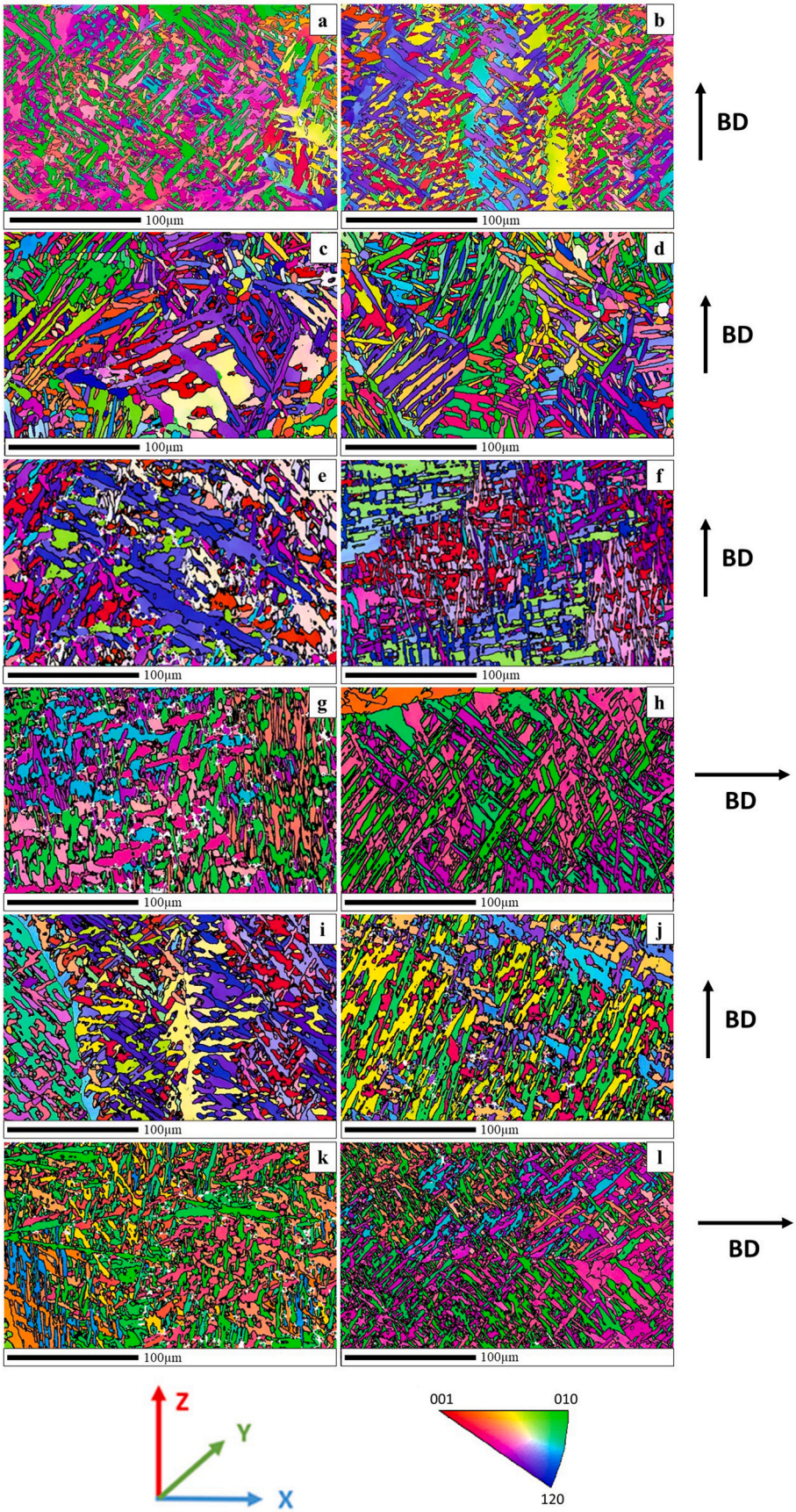

Fig. 3. EBSD IPF maps of Ti–6Al–4V material **a)** EBM vertical X–Y, **b)** EBM vertical X-Z, **c)** L-PBF vertical X–Y, **d)** L-PBF vertical X-Z, **e)** LMD-w parameter set 1 vertical X–Y, **f)** LMD-w parameter set 1 vertical X-Z, **g)** LMD-w parameter set 1 horizontal X–Y, **h)** LMD-w parameter set 1 horizontal X-Z, **i)** LMD-w parameter set 2 vertical X–Y, **j)** LMD-w parameter set 2 vertical X-Z, **k)** LMD-w parameter set 2 horizontal X–Y, **l)** LMD-w parameter set 2 horizontal X-Z.

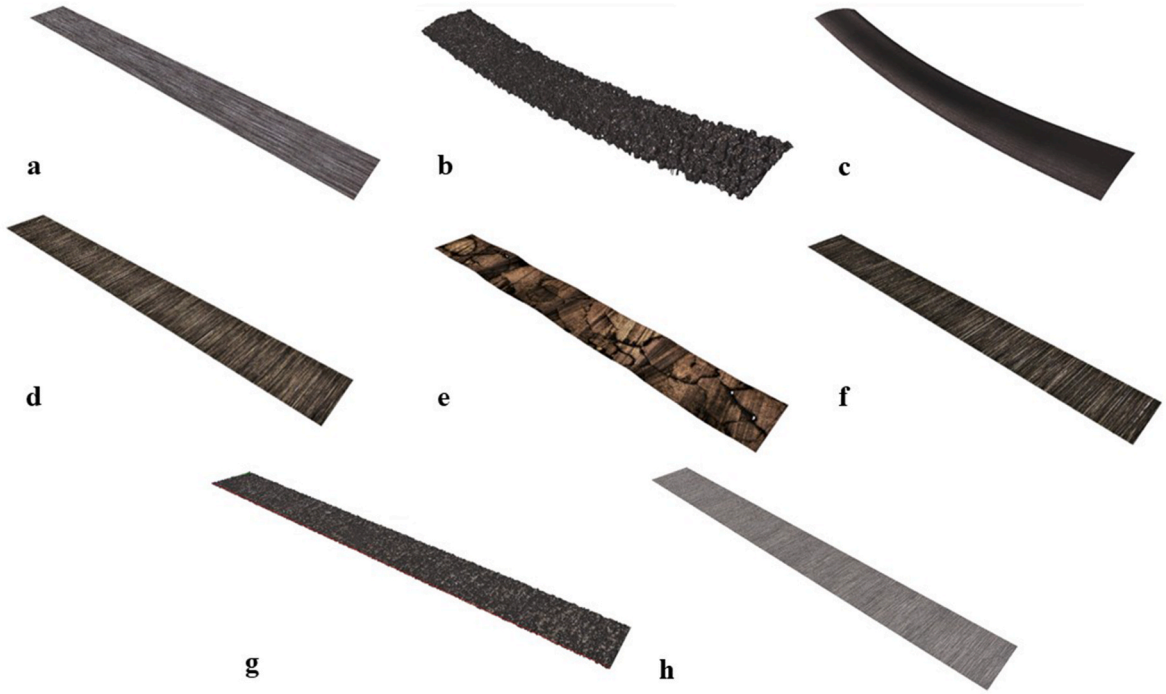

Fig. 4. Alicona surface roughness profiles for AM Ti–6Al–4V samples **a)** conventional machined & polished finish, **b)** EBM as-built surface, **c)** EBM machined & polished finish, **d)** LMD-w parameter set 1 machined & polished finish, **e)** LMD-w parameter set 2 as-built surface, **f)** LMD-w parameter set 2 machined & polished finish, **g)** L-PBF as-built surface and **h)** L-PBF machined & polished finish.

Table 7
Mean average surface roughness parameters generated from Alicona surface profiling for the various AM Ti–6Al–4V variants (M&P = Machined and polished; AB = As-built).

Manufacturing Process	Surface Condition	Orientation	R_a (μm)	R_t (μm)	R_p (μm)	MR^2 (%)	R_v (μm)	S_a (μm)
Conventional (Ax)	M&P		0.8	9.86	5.71	90.22	4.14	1.61
EBM	AB	V	34.79	232.71	107.7	88.5	126.19	191.9
EBM	M&P	V	2.29	8.66	2.46	89.8	6.36	220.32
LMD-w PS1	M&P	V	0.55	4.48	2.14	89.17	2.34	138.99
LMD-w PS1	M&P	H	0.67	6.66	3.56	89.95	3.09	1.27
LMD-w PS2	AB	V	2.06	22.64	9.99	86.96	12.65	50.8
LMD-w PS2	M&P	V	0.97	10.16	4.39	88.25	5.78	1.15
LMD-w PS2	AB	H	2.15	20.73	10.85	90.14	9.88	26.28
LMD-w PS2	M&P	H	1.41	16.29	7.45	87.32	8.84	1.57
L-PBF	AB	V	9.37	66.66	34.68	92.53	31.98	10.11
L-PBF	M&P	V	0.59	6.39	3.64	90.32	2.75	0.67

investigated [35]. They found that generally samples tested using the 4 PB method had a greater fatigue performance than those tested using the axial fatigue test method. This aligns with the results reported by Shrestha et al. and it could therefore be derived that axial fatigue testing provides a more conservative method of fatigue life estimation. As mentioned within this research, a number of 4 PB fatigue tests were completed to estimate the fatigue life of LPBF Ti–6Al–4V samples with various surface finishes. Equivalent samples were not tested using the axial fatigue testing method. In a previous study, Kahlin et al. manufactured a series of uniaxial Ti–6Al–4V samples on a similar EOS M290 machine, and generated results using the same testing conditions as those used within this programme of work [36]. A comparison of the results illustrates that the AB vertical L-PBF fatigue results are highly comparable, despite the different test approaches, but there is a deviation when comparing the M&P vertical results generated from the two sources where the 4 PB results generated in this research exhibit superior fatigue lives compared to the uniaxial results reported by Kahlin et al., a behaviour similar to that reported by Shrestha et al. [10].

In addition to the difference between bending and uniaxial loading, the geometry of the contrasting uniaxial specimens, in the form of cylindrical and flat plate samples, also needs to be considered. Fatemi and Molaei [37] found that flat plate samples have the potential to buckle during the compressive portion of a loading cycle, despite the geometry being recommended for load-controlled axial fatigue tests in the ASTM standard E606-12 [38]. Yet, despite this issue, such behaviour was not seen in this research due to the tensile nature of the R-ratio employed (R = 0.1).

3.2.1. Fractography

Fractographic images were recorded of a series of the AM Ti–6Al–4V variants tested under the same conditions (σ_{MAX} = 600 MPa). Fig. 6 presents typical fracture surfaces of the EBM material. Fig. 6a) and b) show the nucleation zone of an AB specimen, and Fig. 6c) and d) the initiation point in a M&P sample. The images clearly indicate that in an AB sample, fatigue initiation occurs at the surface, with the main dominant fatigue crack originating from one of several surface breaking initiation zones. This behaviour contrasts with a sample with a M&P surface finish, where the point of initiation occurs from a sub-surface, process-induced artefact, that subsequently propagates radially, as indicated by the halo effect, until the crack reaches the edge of the

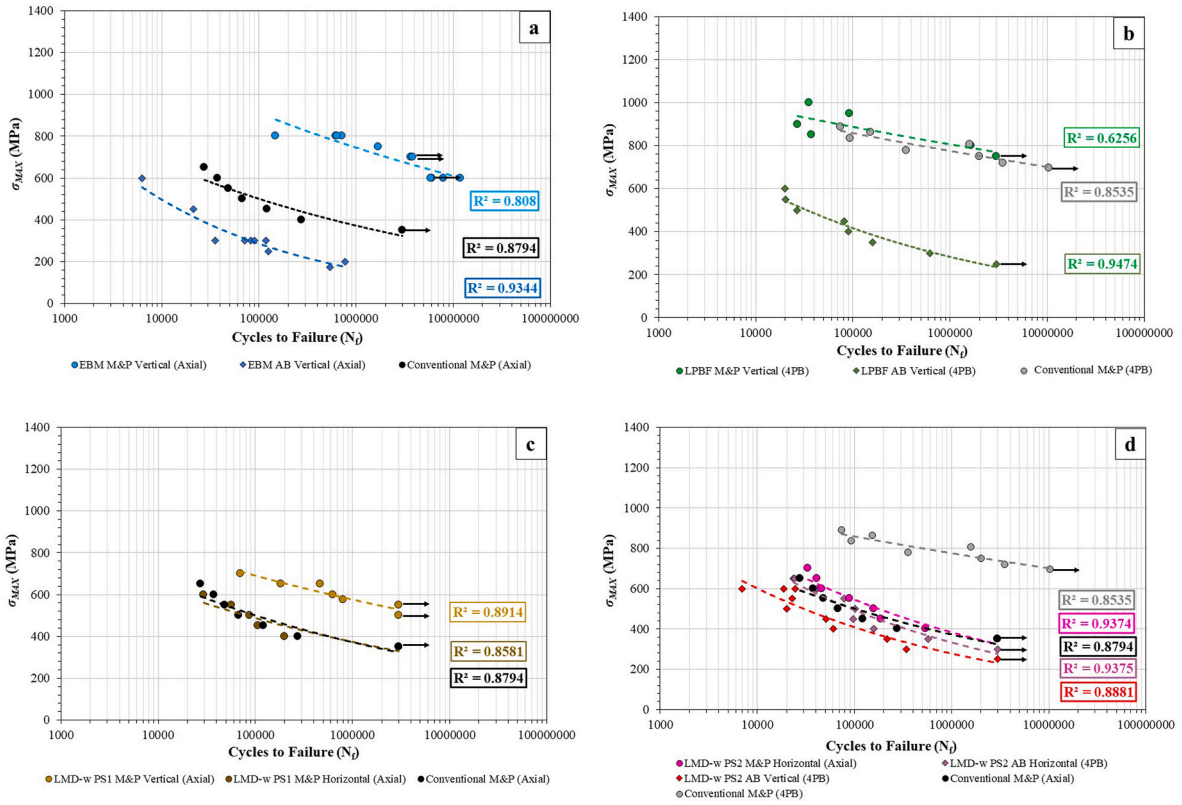

Fig. 5. Fatigue results for a) EBM, b) L-PBF, c) LMD-w PS1, and d) LMD-w PS2 Ti–6Al–4V specimens. Conventional 4 PB fatigue data sourced from Ref. [25].

Table 8
Fatigue lives of AM Ti–6Al–4V specimens tested at $\sigma_{MAX} = 600$ MPa.

Specimen Type	Fatigue Life ($\sigma_{MAX} = 600$ MPa)
L-PBF M&P V (4 PB)	Run out at 10^7 cycles
EBM M&P V (Axial)	6,092,199
LMD-w PS1 M&P V (Axial)	630,147
LMD-w PS2 M&P H (Axial)	46,173
LMD-w PS2 AB H (4 PB)	41,032
Conventional M&P (Axial)	37,724
LMD-w PS1 M&P H (Axial)	29,280
LMD-w PS2 AB V (4 PB)	24,755
L-PBF AB V (4 PB)	20,104
EBM AB V (Axial)	6284

sample. Furthermore, from this set of images the different surface finishes can be seen, in particular the rough surface resulting from partially sintered powder particles in the AB specimen in Fig. 6a). As documented earlier, the M&P surface of EBM samples still exhibits a relatively high effective K_t (2.02) at the surface, despite the removal of a significant amount of surface material. However, this does not seem to have encouraged surface initiation and the difference in fatigue life between the AB and M&P samples is in the order of approximately 1,000x, indicating that the AB surface roughness is very much the driving mechanism on fatigue life in these samples. Furthermore, despite the EBM AB sample exhibiting the highest number of porosity sites amongst the AM Ti–6Al–4V AB variants, there was no evidence of the main dominant crack interacting with any porosity features across the fracture surface.

Similar behaviour can be seen in the L-PBF fracture surfaces, as displayed in Fig. 7. Whereas the AB sample, tested at $\sigma_{MAX} = 600$ MPa, failed after 20,104 fatigue cycles, the M&P sample was tested at a far higher stress ($\sigma_{MAX} = 1000$ MPa) and failed after 35,471 cycles. The two contrasting failure modes can again be seen, with examples of an AB sample given in Fig. 8a) and b), and the M&P equivalents in Fig. 7c) and d). As was the case in the EBM material, for L-PBF, fatigue initiation occurs at the surface of the AB specimen, whilst nucleation occurs at a slightly sub-surface location in the M&P sample. One of the dominant features of the AB fracture surface is again the partially melted powder particles at the surface, which promote a high stress concentration and subsequent reduction in fatigue life. Also found on the surface was an unmelted powder particle (Fig. 7b) which coincides with the PSD of the raw powder feedstock (20–63 μm). Even though such features are understood to be of detriment to fatigue life, there does not appear to be any evidence of the powder particle interacting or influencing the crack growth behaviour. In Fig. 7c) and d), fatigue initiation appears to occur sub-surface from a microstructural feature. The material in this vicinity does not appear to contain any residual defects or artefacts from the manufacturing process, and therefore the presence of any porosity does not seem to be a key influence on fatigue initiation in this material.

Fractographic images of the LMD-w variants are presented in Figs. 8 and 9, for samples from each of the two parameter sets respectively. In Fig. 8, the LMD-w parameter set 2 material follows the same behaviour as that seen in the EBM and L-PBF samples, whereby in the sample with an AB finish, fatigue initiation appears to occur at the surface (Fig. 8a) and b)), as indicated by the surface breaking crack in Fig. 8b). In the M&P sample (Fig. 8c) and d)), prominent features include ductile deformation, a stepped fracture surface and the presence of large porosity sites. The main difference between the two samples is the lack of ductility in the AB sample, as evidenced by the flatness of the surface and the stepped secondary cracking, whilst the M&P sample appears to have failed in a more ductile manner with evidence of gross plasticity.

As found from the porosity measurements in section 3.2.2, the LMD-w parameter set 1 samples appear to be heavily populated in such defects, and this is illustrated in Fig. 9. Fig. 9a)-f) displays typical porosity sites seen in the M&P horizontal samples, three of which (Fig. 9a), e) and f)) have contributed to fatigue nucleation at the surface, and the other three (Fig. 9b), c) and d)) which exhibit a strong presence of porosity, but at more sub-surface locations. Despite the porosity being more

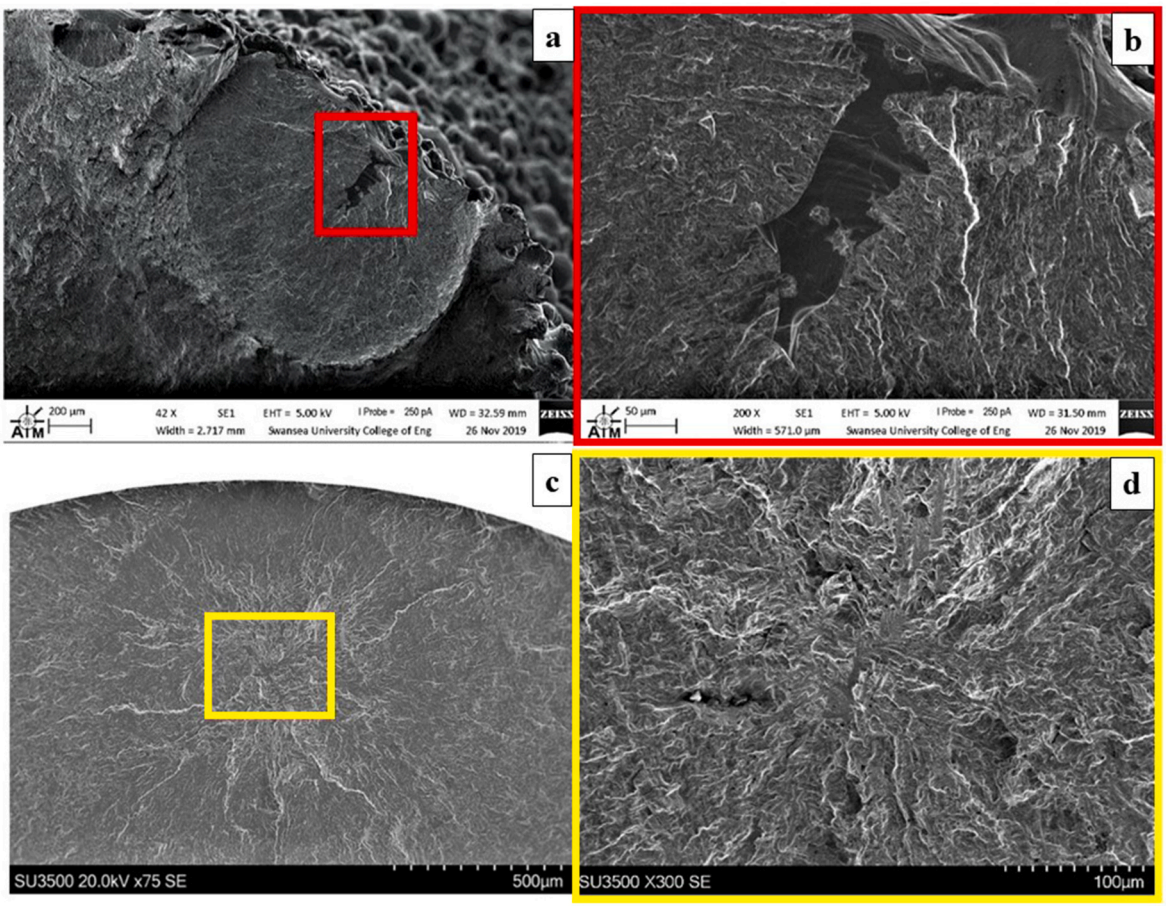

Fig. 6. Fractographic images of EBM Ti–6Al–4V vertical specimens after fatigue testing **a)** as-built surface, **b)** high magnification image of feature in a), **c)** machined & polished finish and **d)** high magnification image of feature in c).

pronounced at the surface in some of the samples, whilst being more evident at internal sites in others, the general S–N curve for this material offered a suitably high R^2 value of 0.94. This suggests that despite the random nature of porosity size, location and population, this does not appear to play a significant role on the resulting fatigue life of this material variant given the relative consistency in the results. This is similarly the case for the LMD-w parameter set 1 vertical specimens, as given in Fig. 9g) and h). Two alternative samples of this material type again exhibit notable porosity sites, each of which fatigue can be seen to initiate from a porosity feature. However, whereas in Fig. 9g), the nucleating porosity site is sub-surface, in Fig. 9h), the initiating site is very much at the surface. Despite the difference in the location of fatigue initiation, again, the R^2 value for the overall S–N curve for this material type is sufficiently high (0.89), suggesting that porosity is not the most significant influencer on fatigue behaviour.

4. Discussion

4.1. Surface roughness

It is known that within AM samples with a high surface roughness, that the peaks and valleys upon the surface act as areas of high stress concentration. Pegues et al. carried out a study to determine the fatigue life of a sample using surface parameter data relating to the peaks and valleys within a surface profile and compared their numerically calculated fatigue results to the tested fatigue life of the same samples [39]. As part of this work, Pegues et al. were able to determine a relationship between the surface parameters to calculate an effective stress concentration (K_t) factor through the following relationship:

$$\overline{K_t} = 1 + n\left(\frac{R_a}{\rho_{10}}\right)\left(\frac{R_t}{R_z}\right) \quad (1)$$

This relationship determines the effective K_t value based on the surface parameters R_a, R_t and R_z along with ρ_{10} which refers to the average radius of a surface valley. n accounts for any changes in stress state, but is typically $n = 1$ for shear, and $n = 2$ for tension. Previous research has related the ρ_{10} value to the average powder radius from the feedstock's powder size distribution since this relationship considers the shape of the valley to determine the numerical stress concentration factor [9]. Here, a ρ_{10} value of 36 µm was used for the EBM samples, and ρ_{10} of 20.75 µm for the L-PBF samples. Due to the proprietary nature of the LMD-w process, a wire diameter was not provided, therefore the upper end of the PSDs used to manufacture other samples within the study has been used to provide a conservative estimation. Therefore, a radius value of 51 µm has been used for the LMD-w samples, indicating that the wire would have a radius of 100 µm. Using this relationship, effective K_t values could be calculated and are displayed in Table 9.

From the numerically calculated effective K_t values it can be seen that the M&P samples all have an effective value of between 1.07 and 1.30, illustrating the consistency of the surface finishes in all cases, irrespective of the manufacturing process used. The one exception to this is the M&P EBM sample, which had an effective K_t of 2.02. This would suggest that despite the machining and polishing stages of these samples removing 760 µm of surface material, this is deemed to be insufficient as stress raising features still remain at the surface. This is also reflected when considering the effective K_t values for samples remaining with an

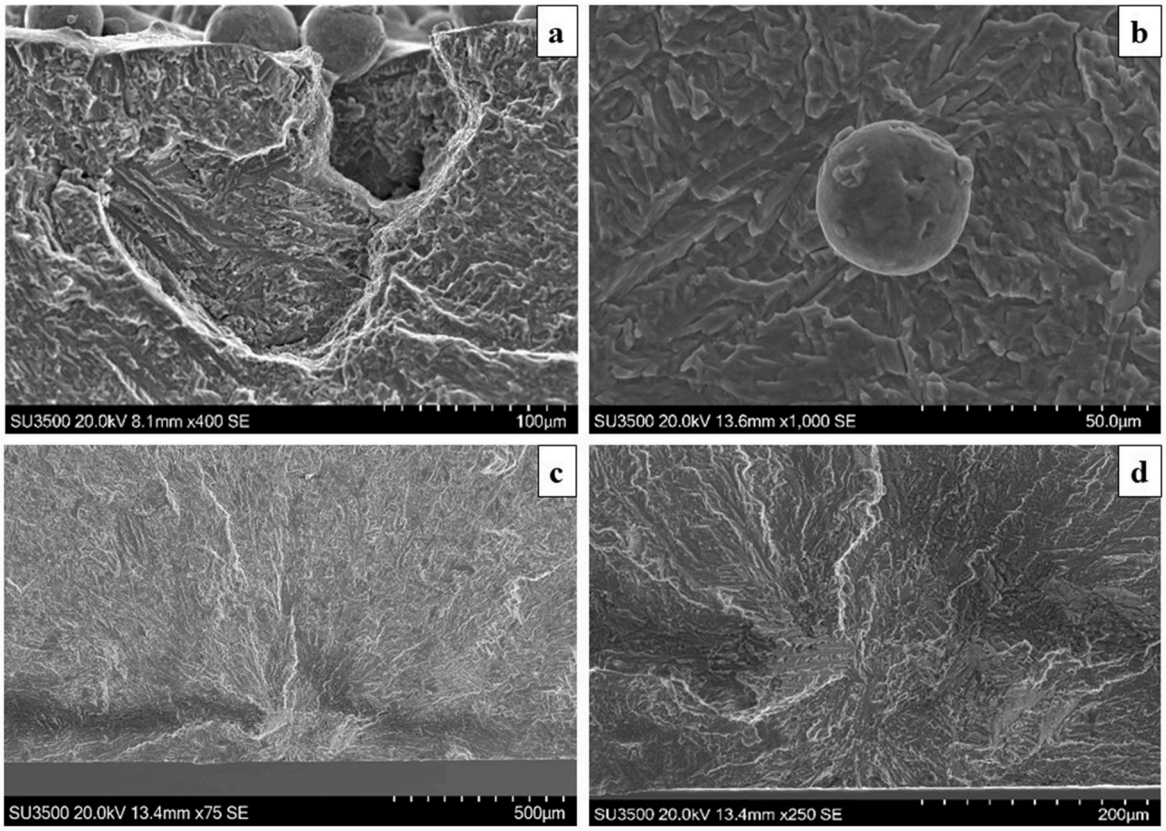

Fig. 7. Fractographic images of L-PBF Ti–6Al–4V vertical specimens after fatigue testing **a), b)** as-built surface, **c), d)** machined & polished finish.

AB surface. Whereas the LMD-w variants both offer a favourable effective K_t, this value rises significantly for the L-PBF material to 5.21, and then increases by almost a factor of 3 for the EBM material, where the AB surface has an effective K_t of 14.31. As such, it would be expected that the considerably high effective K_t of the AB EBM samples would have a significant effect on the fatigue properties.

Nguyen et al. [6] previously observed a similar behaviour when considering the AB surface roughness of comparable AM processes. They also found that, in general, DED based processes, like LMD-w, produce components with the smoothest AB surface finish, which is followed by L-PBF and then EBM. The reasons for the variance stems from the nature of the different AM processes and the contrasting thermal interactions during the manufacturing procedures, such as the interactions of the melt pool and laser or electron power. As EBM and L-PBF tend to keep unused powder particles directly in the powder bed during their respective processes, the LMD-w method simply melts a wire feedstock in-situ, thus there is no loose or partially melted powders in the final component as compared to the EBM and L-PBF techniques. In terms of L-PBF as compared EBM, the coarser surface finish of EBM components is due to the higher thermal radiation associated with the high energy electron beam used in the process, which subsequently leads to an increased adhesion of partially melted powders. In fact, Tuomi et al. [40] actually found that the R_a value of AB EBM Ti–6Al–4V was more than three times that of L-PBF, akin to the behaviour seen here, as given in Table 7. Nguyen et al. [6] previously reported that the surface roughness of EBM produced components can be estimated to be similar to that of the powder feedstock. As such, it is preferable for a fine PSD be used for EBM manufacture to provide a more optimal finish with reduced stress concentrations.

4.2. Porosity

AM materials are commonly regarded as containing a number of process-induced material defects, due to the nature of the manufacturing process and the build material being exposed to rapid and repeated thermal cycles of heating and cooling to produce samples. The action of these thermal cycles can result in material defects such as porosity, areas of lack of fusion, keyhole-related features and inclusions, which can result in a reduction in the mechanical performance of a material and in particular the fatigue performance, as fatigue cracks initiate at areas of high stress concentration such as pores and inclusions [34,41].

To understand the population of porosity features in the different AM variants, images were taken and measurements recorded of any porosity sites found in a series of specimens manufactured through the different AM processes, all of which were mechanically tested under the same loading conditions ($\sigma_{MAX} = 600$ MPa). This was achieved by sectioning through the cross sections of the different samples, metallographically preparing the offcuts and analysing the resulting materials using the Zeiss Smartzoom 5 microscope, as detailed in Section 2.2.2. For each specimen that was analysed, the defect content was recorded from three different regions: A (bottom of the sample in close proximity to the build plate), B (from the approximate mid-point of the failed sample) and C (near the fracture zone of the respective sample).

Fig. 10 displays typical stitched micrographic images of LMD-w samples with an AB and M&P finish manufactured with the two different parameter sets, from which porosity data was measured, and Tables 10 and 11 present the resulting porosity values for the AM samples with an AB and M&P finish, respectively.

From the data shown in Table 10 it can be seen that the porosity count varies greatly, depending on the AM process employed. The highest number of porosity sites is seen in the EBM sample, which coincidentally also exhibited the largest knockdown in fatigue life compared to the machined & polished equivalent. While the EBM sample has the highest level of porosity in the AB samples, similar levels of porosity are seen in the two LMD-w parameter set 2 samples, with these samples exhibiting an average porosity count of 19 and 17 pores

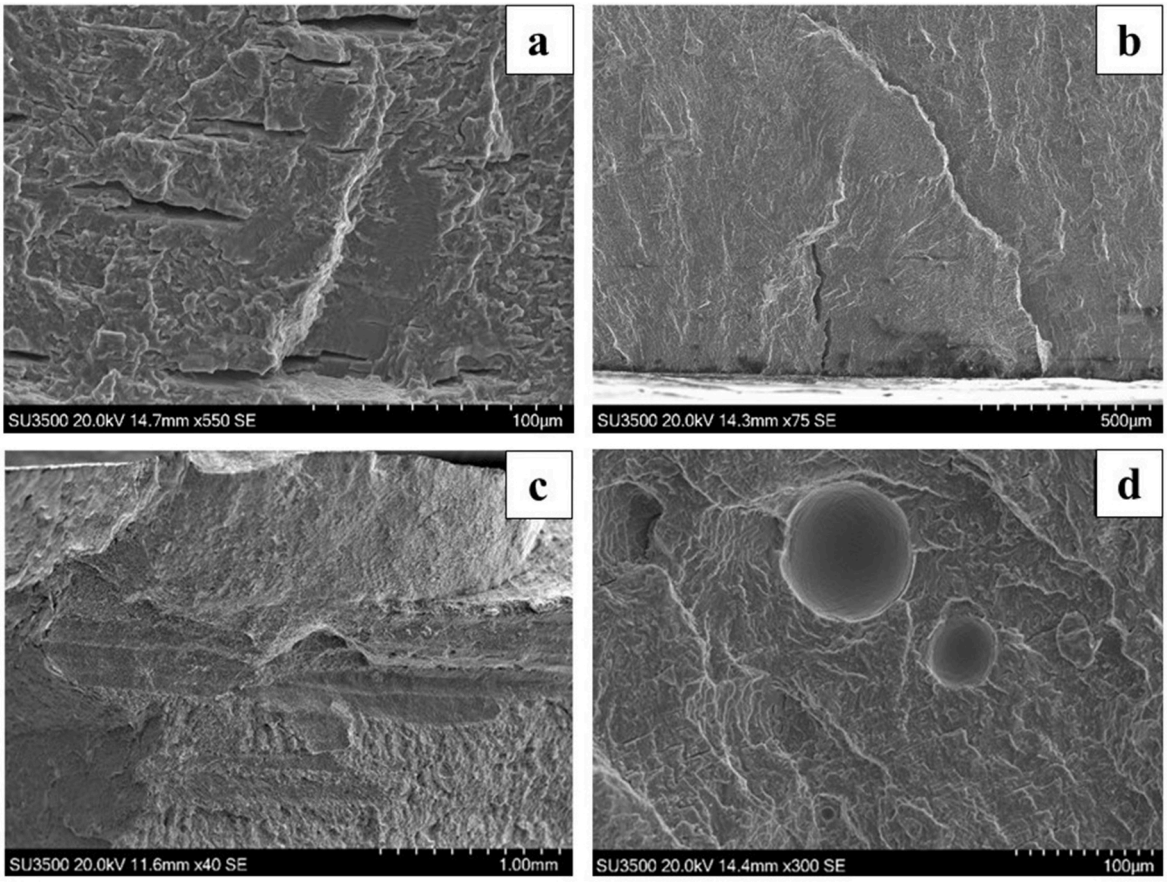

Fig. 8. Fractographic images of LMD-w parameter set 2 Ti–6Al–4V vertical specimens after fatigue testing **a), b)** as-built surface, **c), d)** machined & polished finish.

respectively. Yet despite the LMD-w parameter set 2 samples exhibiting the lowest average porosity count, the largest pore by area seen across all of the variations is seen in the LMD-w parameter set 2 AB horizontal sample, with an area of 6113 μm^2 and a mean average Feret diameter of 69 μm. Likewise, there was also a significant difference in the fatigue lives of the two samples, where the horizontal sample achieved almost six times the fatigue life of the vertical equivalent, despite having a considerably larger pore. Of course, it is difficult to draw a meaningful conclusion from this study and the influence that such features have on the respective fatigue lives since the porosity measurements were recorded from sections within the material and not the actual fracture region, but they do provide an indication of the residing defect population in the contrasting material variants. Details of the fracture behaviours of the AM variants are given in section 3.2.3.

Table 11 presents the equivalent data for a selection of the M&P samples as manufactured through the different AM processes and tested under the same loading conditions (σ_{MAX} = 600 MPa). Note that an L-PBF sample is not included here as no samples were tested under these conditions due to their superior fatigue performance. From the data shown in Tables 11 and it can be seen that the lowest average porosity count was expectedly found in the conventional material, followed very closely by the LMD-w parameter set 2 M&P horizontal sample. Both samples had minimal porosity, but interestingly, for this specimen type, this material exhibited some of the lowest fatigue lives of the samples analysed. Only the LMD-w parameter set 1 horizontal failed after a lower amount of fatigue cycles, despite exhibiting the largest number of pores.

A LMD-w parameter set 1 horizontal sample with a M&P finish was compared to the parameter set 2 samples with either an AB or M&P finish, built in either the horizontal or vertical orientation. This analysis revealed that the parameter set 1 horizontal sample with the M&P finish achieved on average more than twice the fatigue life (120,650 compared to 44,754 (H M&P), 51,242 (H AB) and 77,492 (V M&P), respectively) than the LMD-w parameter set 2 samples, despite having a significantly greater number of porosity sites (average porosity count of 140 compared to 2, 2 and 5) and a significantly higher porosity area. Therefore, this again indicated that porosity content, of the magnitudes found in this research, are not found to be significant drivers in reducing the fatigue performance of AM Ti–6Al–4V materials. Likewise, the microstructures of the different variants were not found to be significantly different, with the average grain size between the LMD-w materials manufactured with the two alternative parameter sets varying by less than 0.3 μm, and the average α lath width being almost the same. Furthermore, the aspect ratios of the orthogonal planes in each variant displayed a similar level of anisotropy, as was also seen in the EBM and L-PBF materials, with an elongated columnar grain structure prominent on the face parallel to the build direction, and a more equiaxed morphology present on the X–Y face.

With this data, it can be seen that there is no trend with the levels of porosity or the average Feret diameter, with significant variations seen across the different sample geometries. The main observation regarding the average Feret diameter is seen within the EBM AB samples, which has the smallest average Feret diameter, yet this sample also has the lowest fatigue life of all samples tested at 600 MPa. Even though this sample contained pores with the smallest average Feret diameter, the same sample also had the second highest number of pores. Therefore, whilst the pores are small, if they were to be clustered together and coalesce, they would synergistically act as a one large defect with a larger surface area. This effect, together with the high effective K_t value as a result of the AB surface roughness, have combined to significantly reduce the cyclic properties of the EBM material. Therefore, whilst porosity has been found to have an element of impact on the fatigue life of AM materials, it is not expected to be the primary or sole factor in

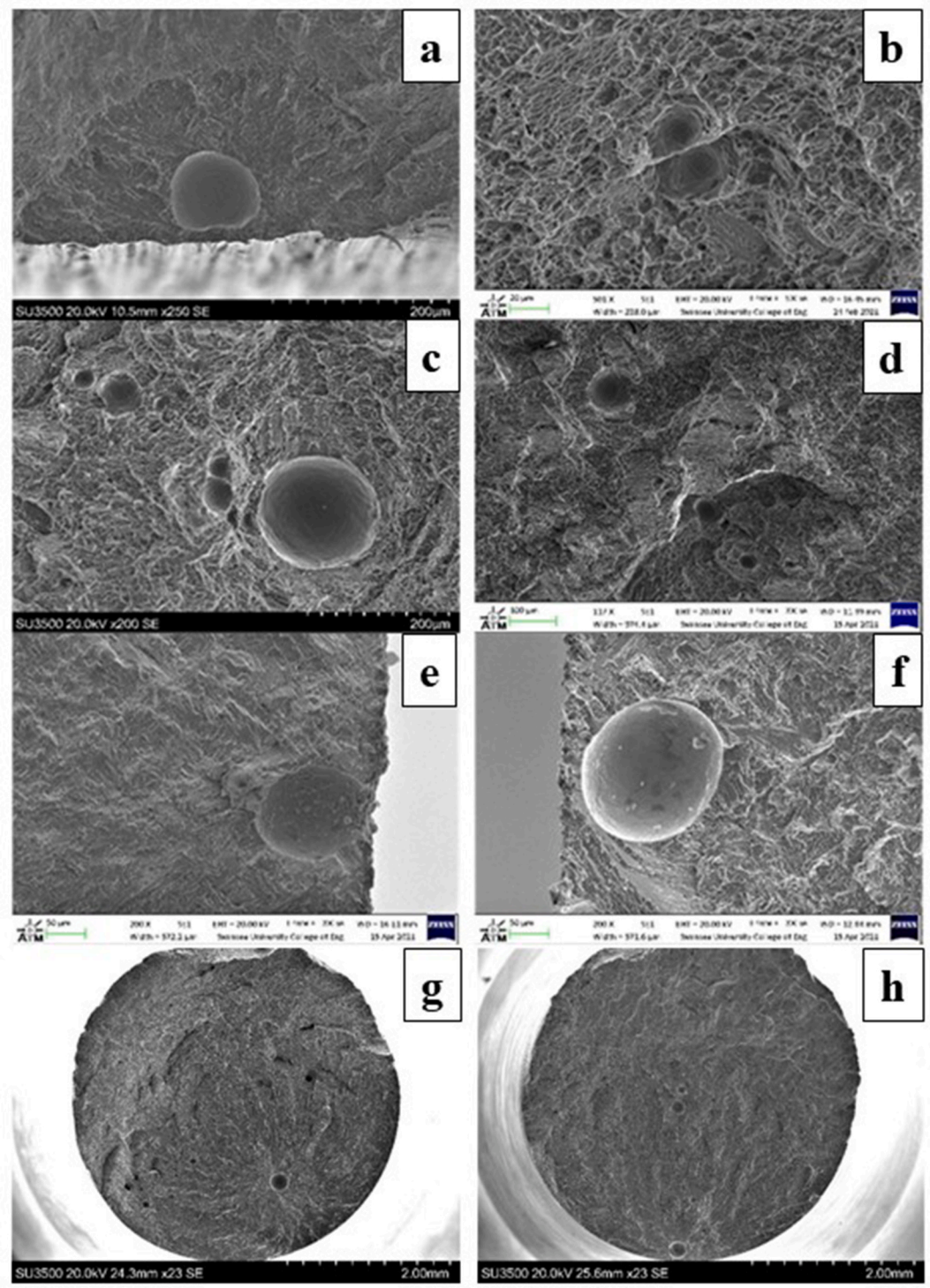

Fig. 9. Fractographic images of LMD-w parameter set 1 Ti–6Al–4V specimens after fatigue testing **a), b), c), d), e), f)** horizontal machined & polished surfaces, **g), h)** vertical machined & polished finish.

influencing the resulting fatigue performance and the stress concentrations at the surface are likely to be of greater importance. Furthermore, a clearer understanding of the role of porosity can be gathered from the post-test fracture surface morphologies and how these features initiate or interact with fatigue damage. To understand this, a selection of the different AM Ti–6Al–4V specimens were subjected to post-tested fractographic studies to identify whether fatigue nucleation occurs at the surface or from sub-subsurface, internal porosity locations.

4.3. Statistical analysis

Applying statistical analysis methods to experimental fatigue data allows for greater interpretation of the experimental results as statistical methods account for unreliability and inconsistencies within the data, whilst also allowing for the prediction of fatigue lives outside the experimental results generated. Statistical analysis was completed on all σ_{MAX}-N_f curves generated on the various AM Ti–6Al–4V materials, using the procedure outlined in ASTM standard E739-10 for 'Statistical

Table 9
Numerically calculated effective K_t values for AM Ti–6Al–4V samples.

Specimen Type	Effective K_t Value
EBM AB Vertical	14.31
EBM M&P Vertical	2.02
L-PBF AB Vertical	5.21
L-PBF M&P Vertical	1.09
LMD-w PS1 M&P Vertical	1.07
LMD-w PS2 M&P Horizontal	1.09
LMD-w PS2 AB Horizontal	1.19
LMD-w PS1 M&P Horizontal	1.09
LMD-w PS2 AB Vertical	1.30

Analysis of Linear Stress-Life and Strain Life Fatigue Data' [42]. The model was modified to determine the Basquin equation constants (b and σ'_f) and subsequently fit the Basquin curve to the experimental fatigue data. It should be noted that within this analysis, tests that reached the applied run out N_f value (3,000,000 cycles) were not considered.

The shape of an S–N curve can be described by Ref. [42]:

$$\log N_f = A + B(S) \tag{2}$$

Where S refers to the maximum value of constant amplitude stress, and A and B refer to the intercept and slope of the linearised model, respectively.

It is assumed within equation (2) that logarithms of fatigue life are normally distributed. Therefore, the log life is constant over the range of the independent variables used in testing (scatter of N_f). Log N_f is used as the dependent variable and is denoted as Y, and the independent variable is denoted as X, which in this case is the tested maximum applied stress (σ_{MAX}). This allows for equation (2) to be re-written as:

$$Y = A + BX \tag{3}$$

Since a linearised model can describe the σ_{MAX} - N_f relationship, A

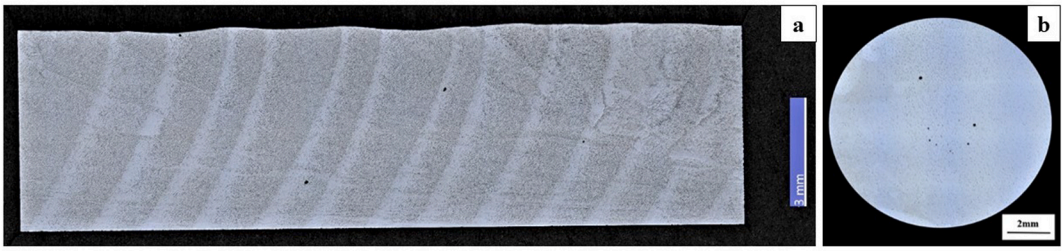

Fig. 10. Sectioned images taken for porosity analysis of **a)** an LMD-w parameter set 2 as-built horizontal sample and **b)** a LMD-w parameter set 1 machined & polished vertical sample.

Table 10
Porosity data for as-built samples tested under equivalent fatigue loading conditions (σ_{MAX} = 600 MPa and R = 0.1). A-C refer to perpendicular sections through the respective specimens at relative locations, where A represents the lowest location and C the highest.

Sample Variation	Section	Test method	N_f	Porosity Count	Mean Average Porosity Count	Mean Average Feret diameter (μm)	Largest pore area (μm^2)	Smallest pore area (μm^2)
EBM vertical	A	Axial	6284	78	70	17.20	406.74	29.76
	B			124		12.78	1863.40	20.19
	C			7		13.73	330.64	19.45
LMD-w PS2 horizontal	A	4 PB	41,032	34	19	30.84	3204.35	19.84
	B			20		12.23	836.94	19.46
	C			5		68.62	6112.94	33.96
LMD-w PS2 vertical	A	4 PB	6960	11	17	15.07	390.76	24.42
	B			35		13.11	904.90	26.14
	C			5		36.54	2346.19	311.23
L-PBF vertical	A	4 PB	20,104	72	34	28.39	1054.35	38.87
	B			25		14.90	219.93	14.34
	C			5		28.94	1478.08	19.32

Table 11
Porosity data for machined & polished samples tested under equivalent fatigue loading conditions (σ_{MAX} = 600 MPa and R = 0.1).

Sample Variation	Section	Test method	N_f	Porosity Count	Mean Average Porosity Count	Mean Average Feret diameter (μm)	Largest pore area (μm^2)	Smallest pore area (μm^2)
Conventional (Axial)	A	Axial	37,724	1	1	51.43	486.97	–
	B			1		11.52	35.72	–
	C			1		34.48	311.30	–
EBM vertical	A	Axial	6,092,199	16	17	34.98	15,177.56	29.82
	B			26		11.28	198.41	19.84
	C			9		62.04	4088.91	35.03
LMD-w PS1 horizontal	A	Axial	29,280	37	30	38.84	9159.60	29.92
	B			44		33.72	8354.01	30.62
	C			10		52.00	7309.41	266.65
LMD-w PS1 vertical	A	Axial	630,147	16	24	42.91	17,049.14	35.51
	B			9		24.76	2342.07	48.09
	C			47		26.34	13,566.67	52.90
LMD-w PS2 horizontal	A	Axial	46,173	3	2	35.69	2780.82	175.09
	B			3		47.60	3140.86	403.46
	C			1		10.10	40.83	–

and B can be estimated using:

$$\widehat{A} = \overline{Y} - \widehat{B}\overline{X} \tag{4}$$

$$\widehat{B} = \frac{\sum_{i=1}^{k}(X_i - \overline{X})(Y_i - \overline{Y})}{\sum_{i=1}^{k}(X_i - \overline{X})^2} \tag{5}$$

Where () refers to an estimate, (¯) refers to the average value, Y_i is equal to $\log(N_f)$, X_i is equal to $\log(\sigma_{MAX})$ and k is the total number of test specimens. Variance within $\log(N_f)$ can be calculated using:

$$\widehat{\sigma}^2 = \frac{\sum_{i=1}^{k}(Y_i - \widehat{Y}_i)^2}{k-2} \tag{6}$$

Calculating the variance within $\log(N_f)$ allows for upper and lower confidence bands for the σ_{MAX}-N_f curve to be calculated using:

$$\widehat{A} + \widehat{B}X \pm \sqrt{2F_p}\widehat{\sigma}\left[\frac{1}{k} + \frac{(X-\overline{X})^2}{\sum_{i=1}^{k}(X_i - \overline{X})^2}\right]^{\frac{1}{2}} \tag{7}$$

In making these calculations and applying them on a $\log(\sigma_{MAX})$ vs $\log(N_f)$ curve alongside experimental data, a median straight line and upper & lower confidence bands can be applied. Using equations (2)–(7), a linearised model can be applied to the fatigue data. From the data calculated using these equations, further derivation can be carried out to calculate the fatigue strength exponent, b and the fatigue strength coefficient, σ'_f, and allowing for the Basquin equation to be applied to experimental fatigue data:

$$\sigma_{MAX} = \sigma'_f\left(2N_f{}^b\right) \tag{8}$$

The Basquin equation describes a power law between the applied stress and the number of fatigue cycles to failure. The Basquin equation constants, b and σ'_f can be calculated as:

$$b = \frac{1}{\widehat{B}} \tag{9}$$

$$\sigma'_f = 10^{-\frac{\widehat{A}}{\widehat{B}}}\left(0.5^b\right) \tag{10}$$

The results of applying both the linearised model outlined by ASTM E739-10 [42] and the fitted Basquin curve for the EBM, L-PBF and LMD-w PS1 and PS2 samples are shown in Figs. 11–14 with the key parameters displayed in Table 12. An indicative example of the linear model is presented in each case to illustrate the upper and lower bounds of the respective fit.

From these results it can be seen that both the linearised model and the corresponding Basquin curves provide a strong agreement with the experimental data for these samples. While in this work, normally distributed linear models and Basquin curves have been successfully applied to experimental fatigue data of AM samples, it is thought that the high levels of scatter in AM fatigue results due to the presence of defects and AB surface roughness should result in non-normal distribution analysis methods being applied, to cover the extremes of the defects found within these samples in combination with normalised distribution methods [43].

As shown in Figs. 11–14 the curve fits using both the linear models and Basquin curves have suitably captured the contrasting data sets. In each case, the graphs can also be used to predict the extended fatigue life of the materials beyond the conditions that were used in this research and provide further upper and lower limits for future tested samples.

5. Conclusions

Within this work the influence of the as-built surface roughness on the stress-controlled fatigue performance of AM Ti–6Al–4V was assessed. Fatigue data has been generated on EBM, L-PBF and LMD-w Ti–6Al–4V samples, with either a machined and polished finish or with an as-built surface. Results have been supported by microstructural analyses, measurements of surface roughness and a characterisation of process-induced defects, whilst considering additional parameters such as build orientation and the manufacturing process, and understanding how each factor affects the resulting fatigue lives. From this research, the following conclusions can be drawn.

- The as-built EBM vertically built samples exhibited the worst fatigue performance, primarily due to the highest process-induced surface roughness of all samples, the highest calculated effective stress concentrations and the subsequent increase of fatigue crack initiation sites at the surface. Furthermore, porosity in the EBM samples were portrayed to be located in clusters and acting synergistically, providing a further knockdown on the fatigue performance.
- Samples built in the vertical orientation typically had a better fatigue performance in the machined & polished condition than the equivalent sample in the horizontal orientation. This is due to the inherent AM grain orientation in vertically built samples that provides a greater resistance to fatigue crack propagation, despite being of a similar size.
- In the as-built condition, horizontally built samples outperformed the vertical equivalent, and therefore a form of orientation dependency exists when the material remains in the as-built surface

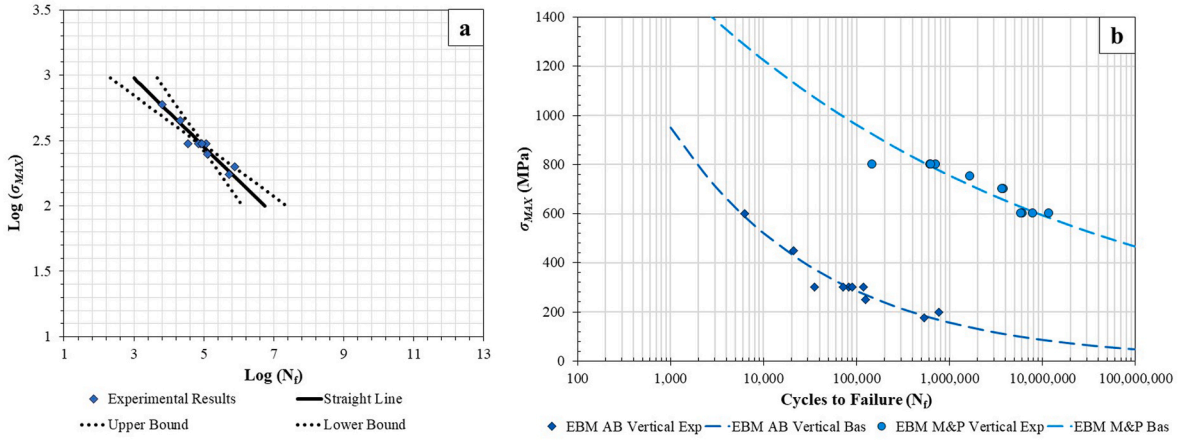

Fig. 11. Statistical analysis of EBM Ti–6Al–4V samples (a) linear model of as-built samples and (b) Basquin predictions.

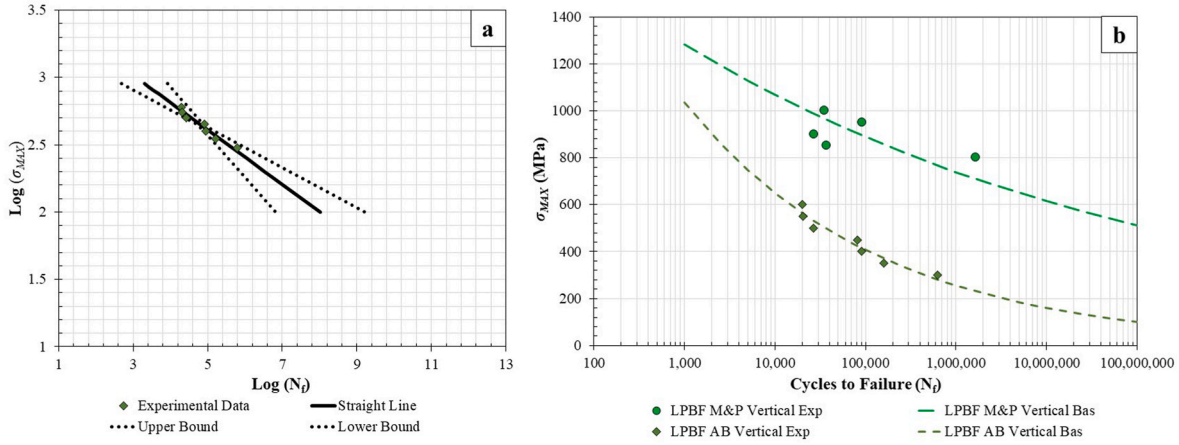

Fig. 12. Statistical analysis of L-PBF Ti–6Al–4V samples (a) linear model of as-built samples and (b) Basquin predictions.

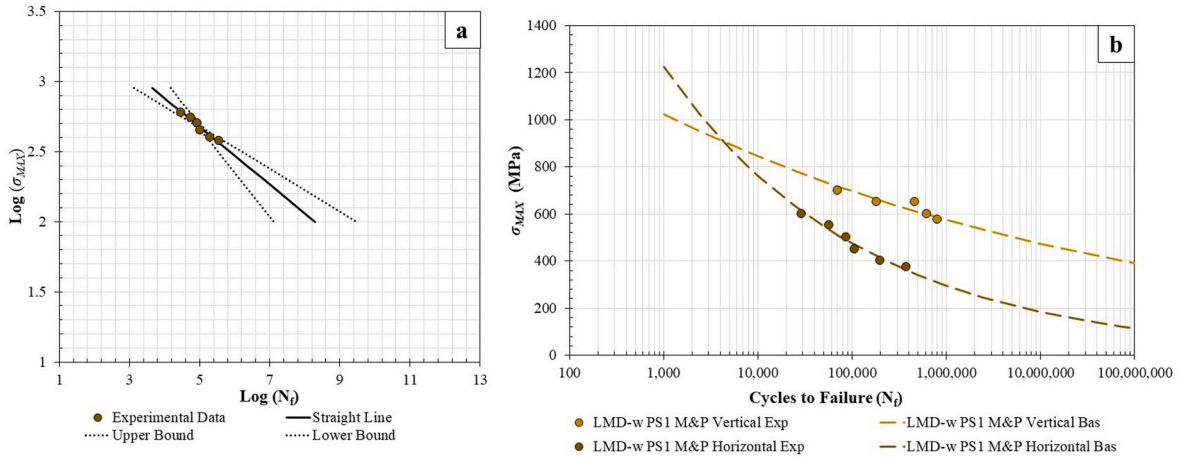

Fig. 13. Statistical analysis of LMD-w PS1 Ti–6Al–4V samples (a) linear model of machined & polished vertical samples and (b) Basquin predictions.

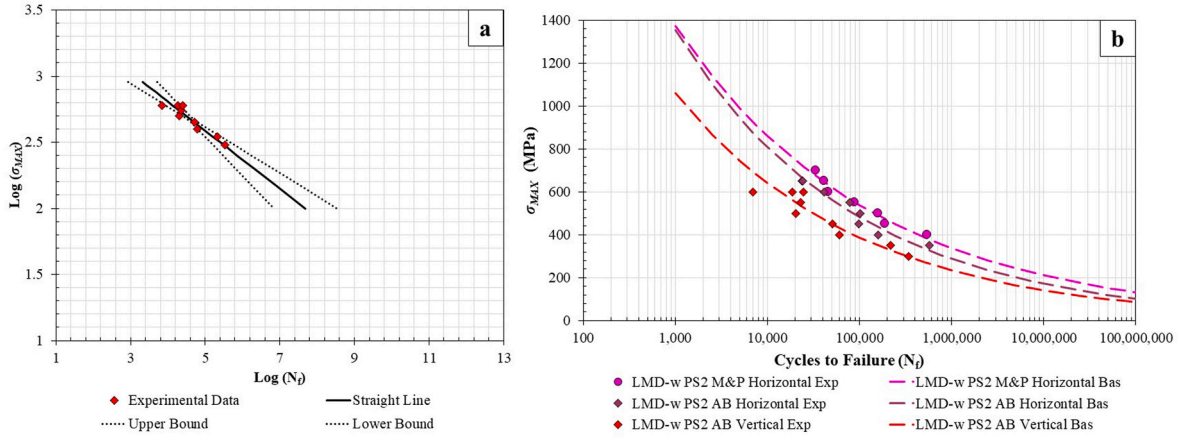

Fig. 14. Statistical analysis of LMD-w PS2 Ti–6Al–4V samples (a) linear model of as-built vertical samples and (b) Basquin predictions.

condition. This was revealed when comparing the fatigue lives of the LMD-w parameter set 2 material, where the horizontal material exhibited a superior fatigue performance compared to the vertical equivalent, with the reason attributed to the nature of the AM process and the staircasing effect that can occur in vertically built samples during manufacture creating a higher stress concentration at the surface.

- Whilst defects and porosity were found to have some impact on the fatigue life of AM material, it was identified to not necessarily be the primary impacting factor. Instead, the as-built surface roughness was found to have the greatest influence, with fatigue initiating at the surface in all samples with an as-built finish. As found from effective stress concentration calculations, the as-built surface roughness of EBM ($K_t = 14.31$) and L-PBF ($K_t = 5.21$) samples were significantly

Table 12
Key parameters for statistical models applied to as-built sample variations.

Material Type	Surface	k	$\hat{A}$	$\hat{B}$	$\hat{\sigma}^2$	b	σ'_f
EBM V	AB	10	14.38	−3.82	0.035	−0.26	6960.89
LMD-w PS2 H	AB	8	16.98	−4.47	0.016	−0.22	7427.10
LMD-w PS2 V	AB	9	16.84	−4.58	0.036	−0.22	5580.19
L-PBF V	AB	7	17.90	−4.94	0.019	−0.20	4822.64
EBM V	M&P	10	14.38	−3.82	0.035	−0.26	6960.89
L-PBF V	M&P	7	17.90	−4.94	0.019	−0.20	4822.64
LMD-w PS1 V	M&P	5	38.97	−11.95	0.044	−0.08	1937.22
LMD-w PS1 H	M&P	6	18.03	−4.87	0.0064	−0.21	5838.47
LMD-w PS2 H	M&P	7	18.44	−4.92	0.0082	−0.20	6452.12

higher than those found in the LMD-w materials ($K_t = 1.19–1.3$) due to the nature of the respective AM processes.

- The ASTM standard E739-10 'Statistical Analysis Methods for Linear Stress Life and Strain Life Fatigue Data' and the modification to provide Basquin constants b and σ'_f, provide a good analytical fit to the experimental data generated within this programme of work allowing for the determination of the fatigue performance of material at extrapolated lives.

Data availability

The raw/processed data required to reproduce these findings cannot be shared at this time as the data also forms part of an ongoing study.

Declaration of competing interest

The authors declare that they have no known competing financial interests or personal relationships that could have appeared to influence the work reported in this paper.

Acknowledgements

The current research was funded by the Materials and Manufacturing Academy, M2A, supported by the European Social fund through the Welsh Government. The provision of a research bursary, materials and supporting information from GKN Additive is gratefully acknowledged. The assistance provided by the Swansea University AIM Facility and the Welsh Coating and Printing Centre, which was funded in part by the EPSRC, are also much appreciated.

References

[1] Sustainable aviation. Net zero carbon road-map summary report. https://www.sustainableaviation.co.uk/wp-content/uploads/2023/04/SA9572_2023CO2RoadMap_Brochure_v4.pdf; 2023.
[2] DebRoy T, et al. Additive manufacturing of metallic components – process, structure and properties. Prog Mater Sci Mar. 2018;92:112–224. https://doi.org/10.1016/j.pmatsci.2017.10.001.
[3] Obilanade D, Dordlofva C, Törlind P. Surface roughness considerations in design for additive manufacturing - a literature review. Proceedings of the Design Society Aug. 2021;1:2841–50. https://doi.org/10.1017/pds.2021.545.
[4] Lee J-Y, Nagalingam AP, Yeo SH. A review on the state-of-the-art of surface finishing processes and related ISO/ASTM standards for metal additive manufactured components. Virtual Phys Prototyp Jan. 2021;16(1):68–96. https://doi.org/10.1080/17452759.2020.1830346.
[5] Bhushan B, editor. Modern tribology handbook, volume one: surface roughness analysis and measurement techniques. CRC Press; 2000.
[6] Nguyen HD, et al. A critical review on additive manufacturing of Ti-6Al-4V alloy: microstructure and mechanical properties. J Mater Res Technol May 2022;18:4641–61. https://doi.org/10.1016/j.jmrt.2022.04.055.
[7] Fox JC, Moylan SP, Lane BM. Effect of process parameters on the surface roughness of overhanging structures in laser powder bed fusion additive manufacturing. Procedia CIRP 2016;45:131–4. https://doi.org/10.1016/j.procir.2016.02.347.
[8] Maleki E, Bagherifard S, Bandini M, Guagliano M. Surface post-treatments for metal additive manufacturing: progress, challenges, and opportunities. Addit Manuf Jan. 2021;37:101619. https://doi.org/10.1016/j.addma.2020.101619.
[9] Beard W, Lancaster R, Barnard N, Jones T, Adams J. The influence of surface finish and build orientation on the low cycle fatigue behaviour of laser powder bed fused stainless steel 316L. Mater Sci Eng, A Feb. 2023;864:144593. https://doi.org/10.1016/j.msea.2023.144593.
[10] Shrestha R, Simsiriwong J, Shamsaei N. Fatigue behavior of additive manufactured 316L stainless steel parts: effects of layer orientation and surface roughness. Addit Manuf Aug. 2019;28:23–38. https://doi.org/10.1016/j.addma.2019.04.011.
[11] Simonelli M, Tse YY, Tuck C. Effect of the build orientation on the mechanical properties and fracture modes of SLM Ti–6Al–4V. Mater Sci Eng, A Oct. 2014;616:1–11. https://doi.org/10.1016/j.msea.2014.07.086.
[12] Elitzer D, et al. Development of microstructure and mechanical properties of TiAl6V4 processed by wire and arc additive manufacturing. Adv Eng Mater Jan. 2023;25(1). https://doi.org/10.1002/adem.202201025.
[13] du Plessis A, Yadroitsava I, Yadroitsev I. Effects of defects on mechanical properties in metal additive manufacturing: a review focusing on X-ray tomography insights. Mater Des Feb. 2020;187:108385. https://doi.org/10.1016/j.matdes.2019.108385.
[14] Tamayo JA, Riascos M, Vargas CA, Baena LM. Additive manufacturing of Ti6Al4V alloy via electron beam melting for the development of implants for the biomedical industry. Heliyon May 2021;7(5):e06892. https://doi.org/10.1016/j.heliyon.2021.e06892.
[15] Cao S, Zou Y, Lim CVS, Wu X. Review of laser powder bed fusion (LPBF) fabricated Ti-6Al-4V: process, post-process treatment, microstructure, and property. Light: Adv Manuf 2021;2(2):1. https://doi.org/10.37188/lam.2021.020.
[16] Liu Z, He B, Lyu T, Zou Y. A review on additive manufacturing of titanium alloys for aerospace applications: directed energy deposition and beyond Ti-6Al-4V. JOM Jun. 2021;73(6):1804–18. https://doi.org/10.1007/s11837-021-04670-6.
[17] Wysocki B, Maj P, Sitek R, Buhagiar J, Kurzydłowski KJ, Świeszkowski W. Laser and electron beam additive manufacturing methods of fabricating titanium bone implants. Appl Sci 2017;7(7):1–20. https://doi.org/10.3390/app7070657.
[18] BS EN 6072:2010 Aerospace series. Metallic materials. Test methods Constant amplitude fatigue testing. 2010.
[19] Huber O. A new technology for high resolution optical 3D surface metrology in the micro and nanometer range. Geophysical Research 2009;11.
[20] ISO 21920-2:2021 Geometrical product specifications (GPS) Surface texture: profile Part 2: terms, definitions and surface texture parameters. 2021.
[21] ISO 25178-2:2021 Geometrical product specifications (GPS) Surface texture: Areal Part 2: terms, definitions and surface texture parameters. 2021.
[22] ISO 12781-1:2011 Geometrical product specifications (GPS) Flatness Part 1: vocabulary and parameters of flatness. 2011.
[23] ASTM E112-13. Standard test methods for determining average grain size. 2021. p. 2021.
[24] ISO 1099:2017 Metallic materials Fatigue testing Axial force-controlled method. 2017.
[25] Kikuchi S, Yoshida S, Ueno A. Improvement of fatigue properties of Ti-6Al-4V alloy under four-point bending by low temperature nitriding. Int J Fatig Mar. 2019;120:134–40. https://doi.org/10.1016/j.ijfatigue.2018.11.005.
[26] Zhou T, Wu J, Liang Z, Che J, Zhang Y, Wang X. A novel constitutive model for Ti–6Al–4V alloy based on dislocation pile-up theory. Mater Sci Technol Jul. 2017;33(11):1379–87. https://doi.org/10.1080/02670836.2017.1295512.
[27] Lucas JJ, Konieczny PP. Relationship between alpha grain size and crack initiation fatigue strength in Ti-6Al-4V. Metall Trans A Mar. 1971;2(3):911–2. https://doi.org/10.1007/BF02662756.
[28] Rafi HK, Karthik NV, Gong H, Starr TL, Stucker BE. Microstructures and mechanical properties of Ti6Al4V parts fabricated by selective laser melting and electron beam melting. J Mater Eng Perform Dec. 2013;22(12):3872–83. https://doi.org/10.1007/s11665-013-0658-0.
[29] Gockel J, Sheridan L, Koerper B, Whip B. The influence of additive manufacturing processing parameters on surface roughness and fatigue life. Int J Fatig Jul. 2019;124:380–8. https://doi.org/10.1016/j.ijfatigue.2019.03.025.
[30] Greitemeier D, Dalle Donne C, Syassen F, Eufinger J, Melz T. Effect of surface roughness on fatigue performance of additive manufactured Ti–6Al–4V. Mater Sci Technol May 2016;32(7):629–34. https://doi.org/10.1179/1743284715Y.0000000053.
[31] Lee S, Ahmadi Z, Pegues JW, Mahjouri-Samani M, Shamsaei N. Laser polishing for improving fatigue performance of additive manufactured Ti-6Al-4V parts. Opt Laser Technol Feb. 2021;134:106639. https://doi.org/10.1016/j.optlastec.2020.106639.
[32] Qiu C, Panwisawas C, Ward M, Basoalto HC, Brooks JW, Attallah MM. On the role of melt flow into the surface structure and porosity development during selective laser melting. Acta Mater Sep. 2015;96:72–9. https://doi.org/10.1016/j.actamat.2015.06.004.
[33] Javadi H, Jomaa W, Texier D, Brochu M, Bocher P. Surface roughness effects on the fatigue behavior of as-machined Inconel718. Solid State Phenom Dec. 2016;258:306–9. https://doi.org/10.4028/www.scientific.net/SSP.258.306.
[34] Sanaei N, Fatemi A. Defects in additive manufactured metals and their effect on fatigue performance: a state-of-the-art review. Prog Mater Sci Apr. 2021;117:100724. https://doi.org/10.1016/j.pmatsci.2020.100724.
[35] Imam MA, Chu HP, Rath BB. Fatigue properties of titanium alloy Ti–6Al–2Cb–1Ta–0.8Mo. Mater Sci Eng, A Jan. 2002;323(1–2):457–61. https://doi.org/10.1016/S0921-5093(01)01473-3.

[36] Kahlin M, Ansell H, Moverare JJ. Fatigue behaviour of notched additive manufactured Ti6Al4V with as-built surfaces. Int J Fatig Aug. 2017;101:51–60. https://doi.org/10.1016/j.ijfatigue.2017.04.009.
[37] Fatemi A, Molaei R. Novel specimen geometries for fatigue testing of additive manufactured metals under axial, torsion, and combined axial-torsion loadings. Int J Fatig Jan. 2020;130:105287. https://doi.org/10.1016/j.ijfatigue.2019.105287.
[38] ASTM E 606. Standard practice for strain-controlled fatigue testing. Astm; 2010.
[39] Pegues JW, Shamsaei N, Roach MD, Williamson RS. Fatigue life estimation of additive manufactured parts in the as-built surface condition. Material Design & Processing Communications Jun. 2019;1(3). https://doi.org/10.1002/mdp2.36.
[40] Tuomi JT, et al. In vitro cytotoxicity and surface topography evaluation of additive manufacturing titanium implant materials. J Mater Sci Mater Med Mar. 2017;28 (3):53. https://doi.org/10.1007/s10856-017-5863-1.
[41] Günther J, et al. Fatigue life of additively manufactured Ti–6Al–4V in the very high cycle fatigue regime. Int J Fatig Jan. 2017;94:236–45. https://doi.org/10.1016/j.ijfatigue.2016.05.018.
[42] ASTM E739-10. Standard practice for statistical analysis of linear or linearized stress-life (S-N) and strain-life (ε-N) fatigue data. 2015. p. 2015.
[43] Murakami Y, Takagi T, Wada K, Matsunaga H. Essential structure of S-N curve: prediction of fatigue life and fatigue limit of defective materials and nature of scatter. Int J Fatig May 2021;146:106138. https://doi.org/10.1016/j.ijfatigue.2020.106138.